

# Sorting Metrics for Customized Phosphorus Diffusion Gettering

Jasmin Hofstetter, David P. Fenning, Douglas M. Powell, Ashley E. Morishige, Hannes Wagner, and Tonio Buonassisi

**Abstract**—Customized solar cell processing based on input material quality has the potential to increase the performance of contaminated regions of multicrystalline silicon ingots. This provides an opportunity to improve material yield and device efficiency without substantially reducing the overall throughput. Simulations and experiments show that in wafers from the top and border regions of an ingot containing as-grown iron concentrations  $\geq 10^{14} \text{ cm}^{-3}$ , a high concentration of interstitial iron point defects, i.e.,  $\text{Fe}_i$ , remains after standard phosphorus diffusion gettering (PDG), severely limiting electron lifetime and simulated efficiencies of PERC-type solar cells. It is shown that an extended PDG leads to a stronger reduction of  $\text{Fe}_i$  point defects, enabling high-efficiency devices, even on wafers from the red zone of the ingot. However, a satisfactory performance improvement after standard PDG is already achieved on wafers that contain as-grown total iron concentrations  $< 10^{14} \text{ cm}^{-3}$ , making the low-throughput extended PDG process unnecessary for a large fraction of the ingot. We propose using the total iron concentration and the corresponding photoluminescence contrast between grain boundaries and intra-granular regions in the as-grown wafer as a simple sorting metric to determine when extended phosphorus diffusion is warranted.

**Index Terms**—Diffusion processes, gettering, impurities, photovoltaic cells, silicon.

## I. INTRODUCTION

THE strongest driver for reducing the cost of photovoltaic solar energy is increasing the solar-cell efficiency, followed by the reduction of material cost [1], [2]. Multicrystalline silicon (mc-Si) solar cell materials have lower area cost ( $\$/\text{m}^2$ ) than monocrystalline silicon materials, but they usually contain

a higher concentration of performance-limiting defects, iron being one of the most abundant and detrimental [3], [4]. During phosphorus diffusion gettering (PDG), the concentration of interstitially dissolved iron point defects, i.e.,  $\text{Fe}_i$ , can be decreased and minority-carrier lifetime increased in *p*-type mc-Si wafers. However, the response to standard PDG seems to depend strongly on the as-grown Si material quality. Due to the large variation of material performance within a mc-Si ingot and particularly low performance at the borders, the bottom, and the top of the ingot, a large fraction of the ingot is cropped off and excluded from device processing. Nevertheless, a large variation in solar-cell efficiency is usually observed within one batch, often exhibiting a low-efficiency tail [5].

During the past few years, different researchers observed that, compared with standard PDG, P-diffusion followed by a low-temperature anneal can lead to a further reduction of  $\text{Fe}_i$  point defects and enhanced minority-carrier lifetimes and solar-cell performance [6]–[11]. However, such an extended PDG requires longer processing times, therefore decreasing throughput, and it does *not* lead to a noticeable performance improvement for all wafers. Hence, a facile sorting metric is needed to determine an optimal processing route, thereby maximizing material usage, solar-cell efficiency, and throughput.

In previous work, it has been shown that  $\geq 99\%$  of total iron is present in the form of iron silicide precipitates, i.e.,  $\text{FeSi}_2$ , in cast mc-Si [12], [13]. These precipitates are often not effectively removed during standard PDG [14]–[16] and act as a source of detrimental  $\text{Fe}_i$  point defects during high-temperature processing. After standard PDG, the  $\text{Fe}_i$  concentration along the height of an intentionally Fe-contaminated ingot was observed to follow the trend of the total iron concentration in the as-grown ingot [17], [18]. The authors in [17] and [18] suggest that a decreasing gettering efficacy may be related to a deterioration of the crystalline quality toward the ingot top.

In this paper, we confirm experimentally that the efficacy of standard PDG to reduce  $\text{Fe}_i$  point defects in cast mc-Si is mainly determined by the *total* concentration of iron in the as-grown material, as predicted by simulations in previous contributions [16], [19]. Therefore, we propose the as-grown total iron concentration as a possible metric to sort cast mc-Si wafers for tailored processing routes. Additionally, an apparent correlation of the total iron concentration in as-grown cast mc-Si wafers with grain boundary contrast in spatially resolved lifetime maps or photoluminescence (PL) images is also discussed, presenting an opportunity for fast and easy inline sorting for customized processing [20]–[22].

Manuscript received February 6, 2014; revised August 4, 2014; accepted August 6, 2014. This work was supported by the National Science Foundation (NSF) and the Department of Energy (DOE) under NSF CA No. EEC-1041895 and by the DOE under Contract No. DE-EE0005314. The  $\text{Al}_2\text{O}_3$  deposition was performed at the Harvard Center for Nanoscale Systems, a member of the National Nanotechnology Infrastructure Network, which was supported by the National Science Foundation under NSF Award ECS-0335765. CNS is part of Harvard University. This work was also supported by the Feodor Lynen Research Fellowship granted by the Humboldt Foundation. The work of D. P. Fenning was supported by the NSF Graduate Research Fellowship. The work of D. M. Powell and A. E. Morishige was supported by the Department of Defense through the National Defense Science and Engineering Graduate Fellowship Program.

J. Hofstetter, D. M. Powell, A. E. Morishige, H. Wagner, and T. Buonassisi are with the Department of Mechanical Engineering, Massachusetts Institute of Technology, Cambridge, MA 02139 USA (e-mail: jasmin.hofstetter@gmx.de; dmpowell@mit.edu; aemorish@mit.edu; hwagner1@mit.edu; buonassisi@mit.edu).

D. P. Fenning is with Department of Mechanical Engineering, Massachusetts Institute of Technology, Cambridge, MA 02139 USA. He is currently also with the Department of Nanoengineering, UC San Diego, La Jolla, CA 92093 USA (e-mail: dfenning@mit.edu).

Color versions of one or more of the figures in this paper are available online at <http://ieeexplore.ieee.org>.

Digital Object Identifier 10.1109/JPHOTOV.2014.2349736

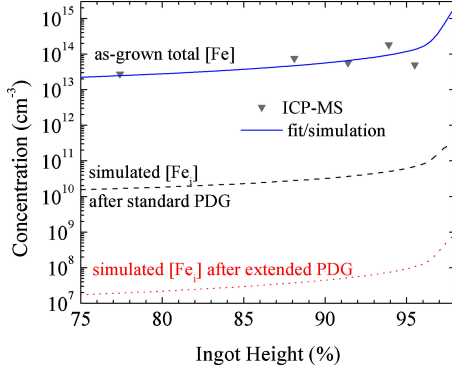


Fig. 1. As-grown total iron concentration along the height of an industrial p-type mc-Si ingot: ICP-MS measurements (triangles) and fitted curve (solid blue line). Dashed and dotted lines are simulated  $\text{Fe}_i$  concentrations after standard and after extended PDG, respectively, assuming an as-grown precipitate radius of 30 nm.

## II. SIMULATION AND EXPERIMENT

### A. Total Iron Concentration

Five samples were selected from the top quarter of a center brick of an industrial p-type cast mc-Si ingot grown from electronic-grade feedstock. Inductively coupled plasma mass spectroscopy (ICP-MS) measurements were performed to determine the total iron concentration along the ingot and are shown as gray triangles in Fig. 1.

The resulting impurity concentration profile is determined by solid-liquid segregation during ingot growth and can be described theoretically by Scheil's equation [23]. Assuming an effective segregation coefficient of iron  $k_{\text{eff,Fe}} = 1.5 \times 10^{-5}$  in mc-Si [24], the ICP-MS data were fit with Scheil's equation, resulting in a total concentration of about  $4 \times 10^{17} \text{ cm}^{-3}$  iron in the melt. After solidification and during crystal cooling, iron from the very top of the ingot diffuses back into the crystal. The back diffusion of iron is simulated assuming an exponential cooling of 17 h with a time constant of 12 h [25]. The resulting calculated total iron concentration profile as a function of ingot height is shown as a solid blue line in Fig. 1.

### B. $\text{Fe}_i$ Concentration and Lifetime

1) *Simulation*: Using the calculated total iron profile as an input, the  $\text{Fe}_i$  concentration profiles after a standard and after an extended PDG along the ingot height are simulated using the *I2E* gettering simulator [26]. The standard PDG consists of a 25-min P-diffusion at 845 °C followed by an exponential cool down to room temperature with a 6-min time constant. The extended PDG consists of a 25-min P-diffusion at 845 °C followed by a slower exponential cool down over 2 h with a 210-min time constant. Simulations are performed assuming an as-grown  $\text{FeSi}_2$  precipitate radius of 30 nm, within the range of sizes that have been observed experimentally in cast mc-Si [14], [16]. The assumption of a constant precipitate size along the ingot height along with other simplifying assumptions in the model (for details, see [19]) only allows for a qualitative

comparison of the simulated and experimental trends in the following.

To estimate the effect of different gettered  $\text{Fe}_i$  concentrations on device performance, a passivated emitter and rear (PERC) solar-cell structure is simulated, using *Sentaurus Device* Version C-2012.06 from *Synopsys Inc.* The parameters of the cell architecture used for the simulation can be found in [27]. The impact of  $\text{Fe}_i$  is modeled via Shockley-Read-Hall (SRH) recombination at a single defect with an energy level at 0.38 eV above the valence band edge and capture cross sections of  $\sigma_e = 1.4 \times 10^{-14} \text{ cm}^2$  for electrons and of  $\sigma_h = 7 \times 10^{-17} \text{ cm}^2$  for holes in the p-type base [28].

2) *Experiment*: From the same brick as mentioned in Section II-A, pairs of  $156 \times 156\text{-mm}^2$  sister wafers, i.e., directly adjacent to each other, were selected from six different ingot heights between 91.3% and 96.3% and cut into smaller samples of about  $4 \times 5 \text{ cm}^2$  in size. All wafers originated from a narrow region of about 2.1 cm close to the top of the ingot. Therefore, they exhibit almost identical grain structure, but the total iron concentration varies by about one order of magnitude. A slight increase in resistivity from about 0.9 to 1.1  $\Omega\text{-cm}$  was measured with increasing ingot height.

Five samples cut from each wafer were saw-damage etched, RCA-cleaned, and double-side surface-passivated with  $\text{Al}_2\text{O}_3$ . The 20-nm-thick  $\text{Al}_2\text{O}_3$  film was deposited in a *Cambridge NanoTech Savannah* atomic layer deposition tool at 200 °C, and a postdeposition anneal at 350 °C was performed in a  $\text{N}_2$  ambient for 10 min. For the resulting film, a surface recombination velocity of  $<10 \text{ cm/s}$  was obtained on a double-side polished FZ test wafer.

The effective electron lifetime of each mc-Si sample was measured with a *Sinton WCT-120* lifetime tester with the samples centered over the coil.  $\text{Fe}_i$  concentrations were determined through the  $\text{Fe}_i\text{-B}_s$  pair dissociation method at an injection level of  $(1\text{--}5) \times 10^{15} \text{ cm}^{-3}$ , which is sufficiently above the crossover point to provide high signal-to-noise ratio [29].

Subsequently, five samples from each ingot height (30 samples in total) were subjected to a standard PDG in a  $\text{POCl}_3$  tube furnace with a time-temperature profile as described in Section II-B1), and the corresponding sister samples (an additional 30 samples) were subjected to an extended PDG.

After PDG, the emitters were etched off, samples were again RCA-cleaned surface-passivated, and the post-processing electron lifetimes and  $\text{Fe}_i$  concentrations were measured. In addition, lifetime maps were measured by scanning microwave-photoconductance decay ( $\mu\text{-PCD}$ ) using a *Semilab WT-2000* tool.

## III. RESULTS

Simulated  $\text{Fe}_i$  concentrations after standard and extended PDG are plotted as dashed and dotted lines in Fig. 1. After standard PDG, the  $\text{Fe}_i$  concentration increases monotonically with increasing total iron concentration, consistent with observations in [18], and varies between  $1 \times 10^{10}$  and  $3 \times 10^{11} \text{ cm}^{-3}$ . After extended PDG, simulations suggest that the  $\text{Fe}_i$  concentration also increases monotonically with increasing total iron

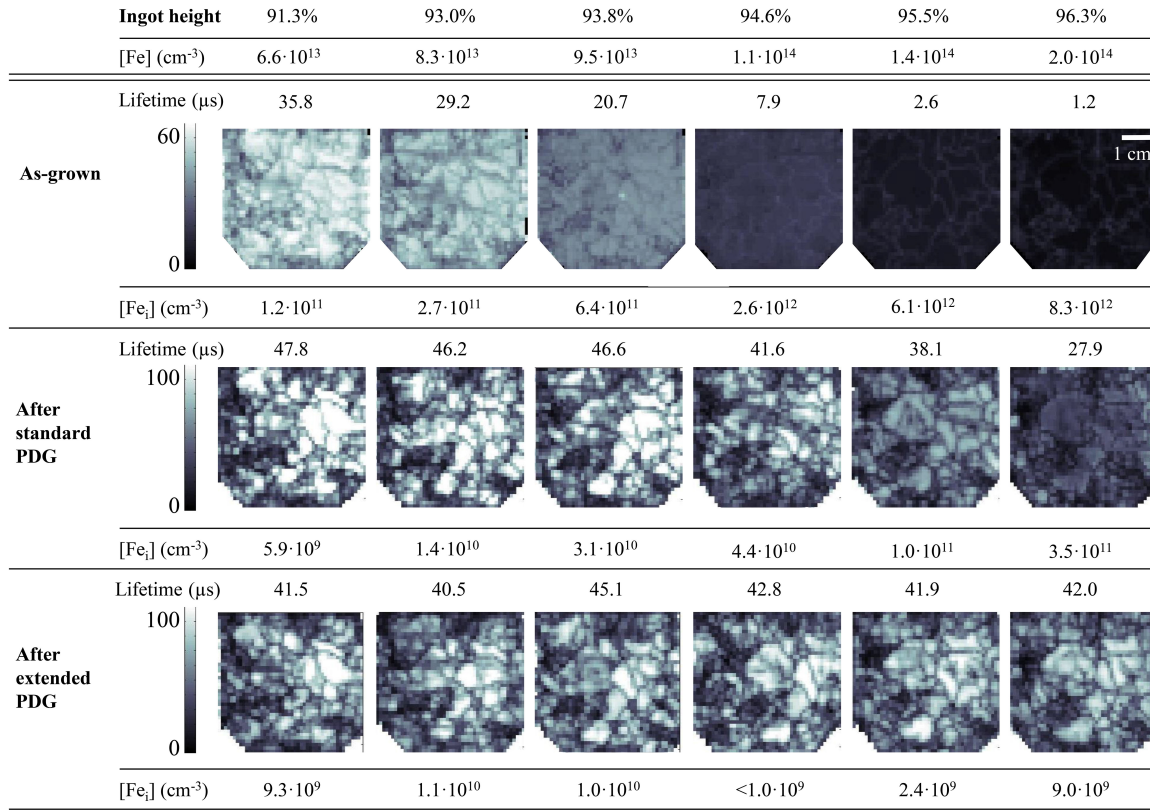


Fig. 2. As-grown total iron concentrations, i.e., [Fe], from 91.3% to 96.3% ingot height extracted from the simulated (blue) curve in Fig. 1. Electron-lifetime maps of one sample per ingot height measured by  $\mu$ -PCD and the respective Fe<sub>i</sub> concentrations, both in the as-grown state and after standard PDG. Note the different scale bars; lifetime maps of as-grown samples have been scaled using a gamma correction factor of 0.6 to allow for a comparison of all the as-grown wafers on the same scale. The lifetime maps of gettering samples are on a simple linear scale. Lifetime maps of the respective sister sample from each ingot height and the respective Fe<sub>i</sub> concentration after extended PDG are also shown. Samples exhibit nearly identical grain structure but show different responses to standard PDG with gettered performance decreasing with increasing ingot height, whereas similar performance is obtained for all ingot heights after extended PDG. Mean lifetimes are given above the respective maps and were calculated as suggested in [30] and described in the text.

concentration but that it is further decreased by several orders of magnitude down to concentrations  $\leq 1 \times 10^9 \text{ cm}^{-3}$  along the entire ingot.

Experimental results are summarized as a table in Fig. 2. In the first two rows, ingot heights and as-grown total iron concentrations, i.e., [Fe], at the respective ingot heights extracted from Fig. 1, are given. Electron lifetime maps of one as-grown sample from each ingot height and its as-grown interstitial iron concentration, i.e., [Fe<sub>i</sub>], are shown. In samples from 91.3 to 93.8% ingot height, grain boundaries exhibit lower lifetimes than intragranular regions, whereas for all three samples further up in the ingot, a denuded zone is observed to develop leading to grain boundaries exhibiting higher lifetimes than the intragranular regions in the low-resolution lifetime maps.

Mean lifetimes were calculated from each map as  $\bar{\tau} = (\frac{1}{N} \sum_{i=1}^N \tau_i^p)^{1/p}$ , where  $\tau_i$  is the lifetime of one pixel,  $N$  is the number of pixels, and  $p = -0.835$ . With increasing ingot height, the calculated mean lifetimes decrease from 35.8 to 1.2  $\mu$ s in as-grown samples. It was shown by Wagner *et al.* [30] that the arithmetic ( $p = 1$ ) or harmonic ( $p = -1$ ) mean lifetime does not show a direct correlation with the solar cell efficiency, but that the most accurate weighting of low and high lifetime regions in multicrystalline wafers is achieved with  $p = -0.835$ .

In the next row, electron-lifetime maps of the same samples are shown after standard PDG. It can be observed that all samples exhibit a nearly identical grain structure. However, the response to standard PDG strongly differs with increasing ingot height. Overall performance decreases with increasing ingot height, i.e., with total iron concentration. Mean lifetimes decrease from 47.8 to 27.9  $\mu$ s. Gettered Fe<sub>i</sub> concentrations for each of these samples are also given and are observed to increase from  $(5.9 \pm 5.1) \times 10^9$  to  $(3.5 \pm 0.1) \times 10^{11} \text{ cm}^{-3}$  with increasing ingot height.

Finally, lifetime maps of the six corresponding sister samples after extended PDG are shown. These maps exhibit very similar lifetime distribution regardless of the ingot height, much in contrast with the maps measured on the respective sister samples after standard PDG. In particular, the overall lifetime increases significantly in the sample from 96.3% ingot height, having the highest as-grown total iron concentration. Mean lifetimes calculated for each map vary slightly between 40.5 and 45.1  $\mu$ s. This indicates that extended PDG improves spatially averaged material performance more uniformly, regardless of the total iron concentration in the as-grown sample. Gettered Fe<sub>i</sub> concentrations for each of these samples are also given and are all  $\leq 1.1 \times 10^{10} \text{ cm}^{-3}$ .



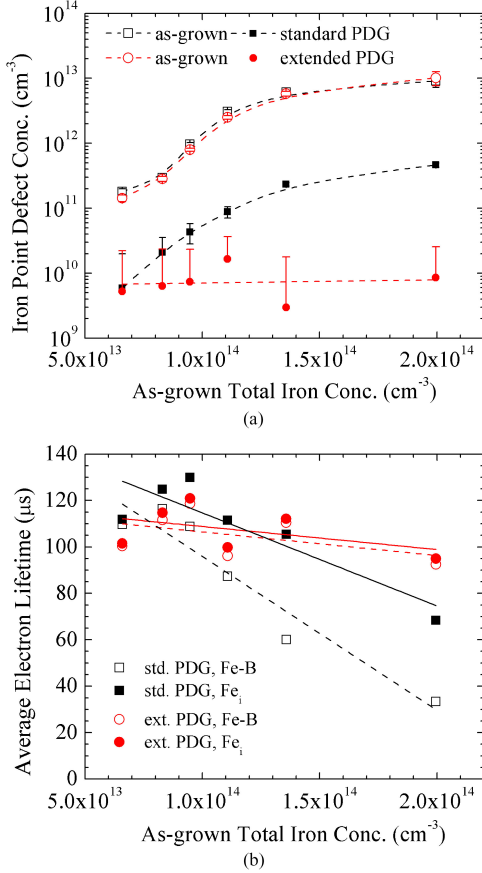


Fig. 3. (a) Average as-grown (open symbols) and post-processing (full symbols)  $\text{Fe}_i$  concentrations after standard gettering (black squares) and after extended gettering (red circles) as a function of the as-grown total iron concentration; after standard PDG, the  $\text{Fe}_i$  concentration increases with the as-grown total iron concentration. After extended PDG, the  $\text{Fe}_i$  concentration is reduced to values at or close to the detection limit for almost all samples. (b) Average post-processing electron lifetime after standard gettering (black squares) and after extended gettering (red circles) at an injection level of  $5 \times 10^{15} \text{ cm}^{-3}$  as a function of the as-grown total iron concentration; full symbols show lifetimes for  $\text{Fe}_i\text{-B}_s$  pairs associated, and open symbols show lifetimes when  $\text{Fe}_i\text{-B}_s$  pairs are dissociated. Lines are guides to the eye.

As-grown and gettered  $\text{Fe}_i$  concentrations averaged over five samples are plotted as a function of the as-grown total iron concentration in Fig. 3(a). The error bars represent the calculated uncertainties summed in quadrature. The uncertainty in the  $\text{Fe}_i$  concentration of each sample has been calculated by assuming a 1.5% relative uncertainty in the lifetime measurements both before and after  $\text{Fe}_i\text{-B}_s$  pair dissociation, accounting for observed variations between measurement repetitions. Any absolute uncertainty in lifetime is assumed to cancel out. Open black squares and red circles represent average  $\text{Fe}_i$  concentrations in the as-grown samples. Concentrations increase monotonically with increasing as-grown total iron concentration, as previously observed and discussed in [12].

Full-black squares in Fig. 3(a) represent average  $\text{Fe}_i$  concentrations after standard PDG, which are reduced by about one order of magnitude in all samples. However, concentrations monotonically increase with the as-grown total iron concentration, consistent with the trend expected from simulations

shown in Fig. 1, and gettered average concentrations between  $6 \times 10^9$  and  $5 \times 10^{11} \text{ cm}^{-3}$  are achieved. In contrast, after extended PDG, average  $\text{Fe}_i$  concentrations are effectively reduced to  $\leq 3 \times 10^{10} \text{ cm}^{-3}$  for all as-grown total iron concentrations, as represented by the full red circles in Fig. 3(a). Within the error of the measurement, equal lifetimes were measured before and after  $\text{Fe}_i\text{-B}_s$  pair dissociation in most of the samples after extended PDG [e.g., see Fig. 3(b)], meaning that the  $\text{Fe}_i$  concentration was too low to be accurately measured with the applied method, as indicated by the large error bars.

In Fig. 3(b), average gettered electron lifetimes measured by quasi-steady-state photoconductance at an injection level of  $5 \times 10^{15} \text{ cm}^{-3}$  are plotted as a function total iron concentration. Lifetimes measured for  $\text{Fe}_i\text{-B}_s$  pairs associated are shown as open symbols, whereas lifetimes measured after  $\text{Fe}_i\text{-B}_s$  pair dissociation are shown as full symbols. After standard PDG, lifetimes decrease with increasing total iron concentration, in particular for total iron concentrations  $> 1 \times 10^{14} \text{ cm}^{-3}$ . After extended PDG, very similar lifetimes are measured for all total iron concentrations, and the gettered lifetime is significantly increased in samples with the highest total iron concentration. For total iron concentrations  $\lesssim 1 \times 10^{14} \text{ cm}^{-3}$ , average lifetimes after extended PDG are comparable or even slightly lower than lifetimes after standard PDG, despite the strongly reduced  $\text{Fe}_i$  concentrations after extended PDG.

In Fig. 4(a), the simulated solar cell efficiency of a PERC structure as a function of the post-processing  $\text{Fe}_i$  concentration is shown for three different lifetimes,  $\tau_{\text{other}}$ , accounting for SRH recombination at other defects apart from  $\text{Fe}_i$ . The total SRH lifetime can, therefore, be written as  $1/\tau_{\text{SRH}} = 1/\tau_{\text{other}} + 1/\tau_{\text{Fe}_i}$ . For the lowest  $\text{Fe}_i$  concentrations, high efficiencies of 20.3%, 20.9%, and 21.4% are reached for the three different lifetimes  $\tau_{\text{other}}$  of 50, 100, and 200  $\mu\text{s}$ , respectively, and the efficiencies are almost independent of the  $\text{Fe}_i$  concentrations. For  $\text{Fe}_i$  concentrations  $\gtrsim 10^{11} \text{ cm}^{-3}$ , the efficiency starts to drop significantly with the reduction being more pronounced for higher  $\tau_{\text{other}}$ . Average  $\text{Fe}_i$  concentrations measured at different ingot heights after standard and extended PDG are denoted as black squares and red dots, respectively.

In Fig. 4(b), the absolute efficiency losses simulated for average  $\text{Fe}_i$  concentrations measured after standard and extended PDG in this study are plotted as a function of the as-grown total iron concentration in the respective samples. After standard PDG, efficiency losses due to the remaining gettered  $\text{Fe}_i$  concentration increase with increasing total iron concentration. The absolute efficiency loss is  $\lesssim 0.2\%$  for total iron concentrations  $< 1 \times 10^{14} \text{ cm}^{-3}$  but increases up to 2.2% for higher total iron concentrations in the as-grown wafer. In contrast, after extended PDG, efficiency losses are  $\lesssim 0.1\%$  independent of the as-grown total iron concentration.

#### IV. DISCUSSION

Lifetime and efficiency results shown in Figs. 2, 3(b), and 4(b) suggest that the as-grown total iron concentration may be an effective sorting criterion for wafers from cast mc-Si ingots to be subjected to standard or extended PDG. During

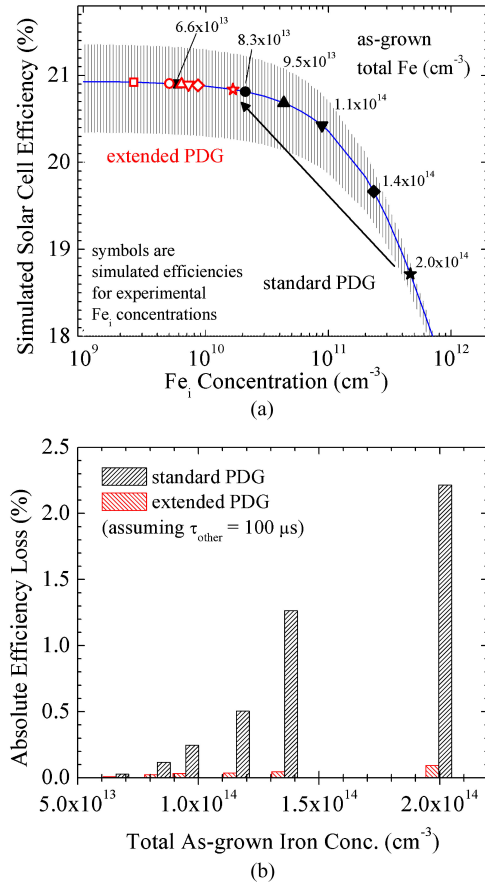


Fig. 4. Impact of the gettered  $Fe_i$  concentration on solar-cell efficiency in a PERC structure. (a) Solar-cell efficiency as a function of the  $Fe_i$  concentration, assuming  $\tau_{other}$  of 100  $\mu s$  (blue line), representing SRH recombination at other defects apart from  $Fe_i$ ; full black and open red symbols denote simulated efficiencies for measured  $Fe_i$  concentrations after standard and extended PDG, respectively, with different symbols denoting different as-grown total iron concentration; the shaded area denotes an efficiency range for  $\tau_{other}$  varying between 50 and 200  $\mu s$ . (b) Absolute solar cell efficiency loss as a function of the as-grown total iron concentration when applying a standard PDG (black columns) or an extended PDG (red columns).

any high-temperature processing step, the dissolution of iron-containing precipitates tends to increase the concentration of  $Fe_i$  point defects up to the solid-solubility limit at the given temperature. At the same time, the diffusion of  $Fe_i$  point defects to the P-diffused wafer surface decreases their concentration in the wafer bulk. A dynamic-equilibrium  $Fe_i$  concentration is established at high temperature [19], and whether precipitate dissolution or the gettering of iron interstitials dominates mainly depends on the kinetics of precipitate dissolution and, therefore, on the concentration of precipitated ( $\approx$ total) iron in the as-grown wafer.

However, the final  $Fe_i$  concentration after high-temperature gettering can be controlled by the cooling step: During a fast cool-down, i.e., when the wafers are pulled out of the furnace at high temperature, the post-processing  $Fe_i$  concentration is determined by the dynamic-equilibrium concentration that establishes at high temperature. In contrast, during a slow cool down, further precipitate dissolution is suppressed, while the diffusiv-

ity of  $Fe_i$  point defects is still high enough to be driven to the P-diffused layer and low  $Fe_i$  concentrations can be achieved, as previously observed by different researchers [7]–[10], [31], [32]. Both trends are reflected in simulations in Fig. 1 and consistent with experimental observations in Figs. 2 and 3(a). First, we find that the post-processing  $Fe_i$  concentration after standard PDG increases with as-grown total iron concentration, consistent with previous experimental observations in [18] and [31]. Second, we find that during an extended PDG,  $Fe_i$  point defects can be effectively removed in all samples to concentrations  $< 3 \times 10^{10} cm^{-3}$ , independent of their as-grown total iron concentration. This finding has been previously indicated in postgettering results along the ingot height in [8], [31], and [32]. In this study, the selection of samples from a very narrow region at the ingot top allows the effect of the varying total metal concentration on gettering efficacy to be isolated: Samples originating from the same ingot height show a very similar gettering response (gettered  $Fe_i$ ) despite exhibiting a very different grain structure and distribution of crystalline defects (not shown). In contrast, sister samples from different ingot heights but with almost identical grain structure show very different response to standard PDG, as shown in Fig. 2.

Consequently, for an industrial cast mc-Si ingot, both experimental and simulation results suggest that wafers can be roughly classified with respect to their as-grown total iron concentrations.

- 1) As-grown iron concentrations  $< 10^{14} cm^{-3}$  are usually found in the center region of cast mc-Si ingots [17], [33], [34]. In these wafers, an efficient reduction of the  $Fe_i$  concentration can be achieved during standard PDG. This  $Fe_i$  reduction leads to increased post-processing electron lifetime and would allow for maximum efficiencies in PERC-type devices with efficiency losses due to  $Fe_i \lesssim 0.2\%$  absolute.
- 2) As-grown iron concentrations  $> 10^{14} cm^{-3}$  are usually found in wafers from the border and top of cast mc-Si ingots, with the affected fraction of the ingot increasing with decreasing purity of the Si melt, of the quartz crucible, and of the crucible lining [12], [17], [34]–[37]. For these lower purity wafers, the dissolution of precipitated iron prevents the decrease of the  $Fe_i$  concentration to sufficiently low values during standard PDG, resulting in poor postprocessed material performance, as shown in Fig. 2. The remaining  $Fe_i$  concentration can lead to efficiency losses in PERC-type devices of up to 2.2% absolute in the present samples, as shown in Fig. 4(b). For such wafers, the addition of a slow cool-down to the PDG step is beneficial and would allow to decrease absolute efficiency losses to  $\lesssim 0.1\%$  independently of the as-grown total iron concentration.

Unfortunately, it is not feasible to accurately determine trace impurity concentrations such as the as-grown total iron concentration in a wafer using mass-spectroscopy techniques in an industrial inline screening process. PL imaging has been suggested as a fast, nondestructive, and noncontact screening method for as-grown wafers [20]–[22]. The suggested sorting criteria are mainly the visibility of highly dislocated regions or

other inhomogeneities in the as-grown wafer such as the low-lifetime “red zone” in wafers from the borders and edges of the ingot.

We have recently suggested [38] that the contrast between grain boundaries and intragranular regions in as-grown lifetime maps or PL images may serve as sorting criteria for customized gettering processes. As observed in as-grown lifetime maps in Fig. 2, the measured electron lifetime in both intragranular regions and around grain boundaries gradually decreases with increasing ingot height. The intragranular lifetime is presumably dominated by point defects and, therefore, degrades with increasing  $\text{Fe}_i$  concentration toward the ingot top. The lifetime measured at grain boundaries also seems to decrease, but, due to the limited spatial resolution of the measurement, it is convoluted with the lifetime in the surrounding area. Thus, the lifetime measured at grain boundaries, which may depend on grain boundary type, orientation, and metal decoration, is assumed to be largely lost in the lifetime signal from a narrow region around the boundary that is denuded of  $\text{Fe}_i$  due to internal gettering to the boundary [39], [40]. The existence of a denuded zone becomes visible in lifetime maps of as-grown wafers from above 94% ingot height. Interestingly, it is exactly these wafers from  $\geq 94\%$  ingot height that benefit from an extended PDG step.

Concluding from these observations, in as-grown wafers from the ingot top in which grain boundaries show a lower lifetime than intragranular regions, i.e., a contrast  $PL_{\text{boundaries}}/PL_{\text{grains}} < 1$ , maximum postgettering performance can be achieved through a high-throughput standard PDG step. However, in as-grown wafers that show a denuded zone around grain boundaries with higher lifetime than intragranular regions ( $PL_{\text{boundaries}}/PL_{\text{grains}} > 1$ ), an extended PDG is required to achieve equally high material and device performance. This criterion is assumed to be applicable to wafers with similar high total iron concentrations from the borders and bottom part of the ingot as well, but further experiments on wafers from these parts of the ingot (and from other ingots) may be required to verify this assumption.

It is also readily observable in Fig. 2 that no significant electron-lifetime improvement seems to be achieved in regions of high dislocation density or along grain boundaries during extended PDG in comparison to standard PDG. It is likely that the electron lifetime there is limited by charge-carrier recombination at  $\text{FeSi}_2$  precipitates or at metal-decorated structural defects [41], [42].

The impact of different processing schemes on  $\text{FeSi}_2$  precipitates in highly iron-contaminated mc-Si has been investigated by means of X-ray fluorescence microscopy ( $\mu$ -XRF) [14], [16].  $\mu$ -XRF results confirm that both standard and extended PDG mainly act on the concentration of interstitially dissolved iron but hardly affect the distribution of precipitated iron. As a consequence, during subsequent high-temperature processes, the dissolution of these remaining precipitates can offset the  $\text{Fe}_i$  reduction achieved during standard and extended PDG if the peak temperature is chosen too high, e.g., during metal-contact firing. However, it has been shown in [43] that the selection of a low peak temperature can prevent degradation during firing, and the addition of a short low-temperature plateau

after the temperature peak can even lead to an additional  $\text{Fe}_i$  reduction.

The effective gettering of regions with high structural defect density is subject to ongoing investigations. PDG at higher temperatures up to 920 °C has recently been shown to lead to an enhanced size reduction of  $\text{FeSi}_2$  precipitates at grain boundaries [44]. It was also found that the reduction of precipitated iron through a high-temperature peak during PDG reduces the detrimental effect of  $\text{Fe}_i$  increase during metal-contact firing, even at a relatively high peak temperature of 900 °C [45].

In previous work, we found that the gettering efficacy not only depends on the as-grown concentration of precipitated iron, but also on its distribution, i.e., the size and density of iron  $\text{FeSi}_2$  precipitates [46], [47]. We also observed that the average precipitate size and density varies along the height of a cast mc-Si ingot. However, the variation over an ingot is small compared with the variation between mc-Si and other c-Si materials (e.g., ribbon and Czochralski). Thus, simulations suggest that the impact of the as-grown total iron variation on the  $\text{Fe}_i$  concentration after standard PDG is larger than the impact of the observed precipitate size variation within a mc-Si ingot [16].

In materials with a very different thermal history than conventional cast mc-Si ingots, e.g., Si ribbon materials that undergo a much faster cooling after crystallization, the size and density of  $\text{FeSi}_2$  precipitates can be very different [48]. This will change the dissolution kinetics of precipitates during high-temperature processing [47] and the effectiveness of internal or relaxation gettering during cooldown. Therefore, the ideal sorting criterion for customized PDG will likely be different for other crystalline silicon materials and may also evolve with increasing mc-Si ingot quality.

## V. CONCLUSION

The impurity content and material quality in mc-Si varies over the ingot; thus, it seems natural to customize phosphorus gettering to the different regions to extract the maximum efficiency potential from each wafer and expand the range of usable material. Present results indicate that in cast mc-Si, the efficacy of standard PDG to reduce the  $\text{Fe}_i$  concentration and, therefore, to potentially increase the electron lifetime and solar-cell efficiency, largely depends on the total concentration of iron in the as-grown wafer. High-throughput standard PDG effectively decreases the  $\text{Fe}_i$  concentration in the majority of wafers from a cast mc-Si ingot with total iron concentration  $< 1 \times 10^{14} \text{ cm}^{-3}$ . However, advanced time-temperature profiles are required to extract the full-lifetime potential of wafers from the very top of the ingot, where the total iron concentration exceeds  $1 \times 10^{14} \text{ cm}^{-3}$ .

Besides the as-grown total iron concentration, the contrast between grain boundaries and intragranular regions in electron lifetime maps appears to be a fairly accurate metric to sort as-grown p-type cast mc-Si wafers from the top of the ingot for standard and advanced PDG processes: An advanced gettering profile should be applied to wafers in which grain boundaries show a denuded zone with higher electron lifetime than intragranular regions. Additional experiments are required to



test if the sorting criterion can be further generalized, e.g., if it applies to wafers from the bottom of the ingot.

Tailored processing would allow solar-cell manufacturers to achieve an optimum tradeoff between material performance and processing throughput for different types of material. A resulting tighter efficiency distribution with a higher mean could narrow the gap between solar cell and module efficiencies, reducing the cost of crystalline Si photovoltaics.

#### ACKNOWLEDGMENT

The authors would like to thank Prof. H. Savin and Dr. A. Akey for helpful discussions, as well as Dr. A. Akey for the critical reading of the manuscript.

#### REFERENCES

- [1] G. del Coso, C. del Cañizo, and W. C. Sinke, "The impact of silicon feedstock on the PV module cost," *Sol. Energy Mater. Sol. Cells*, vol. 94, pp. 345–349, 2010.
- [2] D. M. Powell, M. T. Winkler, H. J. Choi, C. B. Simmons, D. B. Needleman, and T. Buonassisi (2012). Crystalline silicon photovoltaics: A cost analysis framework for determining technology pathways to reach baseload electricity costs. *Energy Environ. Sci.* [Online]. vol. 5, pp. 5874–5883. Available: <http://dx.doi.org/10.1039/C2EE03489A>
- [3] A. Istratov, H. Hieslmair, and E. R. Weber, "Iron and its complexes in silicon," *Appl. Phys. A*, vol. 69, pp. 13–44, 1999.
- [4] T. Buonassisi, A. A. Istratov, M. D. Pickett, M. Heuer, J. P. Kalejs, G. Hahn, M. A. Marcus, B. Lai, Z. Cai, S. M. Heald, T. F. Ciszek, R. F. Clark, D. W. Cunningham, A. M. Cabor, R. Jonczyk, S. Narayanan, E. Sauer, and E. R. Weber, "Chemical natures and distributions of metal impurities in multicrystalline silicon materials," *Prog. Photovoltaics. Res. Appl.*, vol. 14, pp. 513–531, 2006.
- [5] Y. Yang, A. Yu, B. Hsu, W. Hsu, A. Yang, and C. Lan, "Development of high-performance multicrystalline silicon for photovoltaic industry," *Prog. Photovoltaics. Res. Appl.* 2013. DOI: 10.1002/pip.2437.
- [6] J. Härkönen, V.-P. Lempinen, T. Juvonen, and J. Kylmäluoma, "Recovery of minority carrier lifetime in low-cost multicrystalline silicon," *Sol. Energy Mater. Sol. Cells*, vol. 73, pp. 125–130, 2003.
- [7] P. Manshanden and L. Geerligs, "Improved phosphorous gettering of multicrystalline silicon," *Sol. Energy Mater. Sol. Cells*, vol. 90, pp. 998–1012, 2006.
- [8] J. Tan, A. Cuevas, D. Macdonald, N. Bennett, I. Romijn, T. Trupke, and R. Bardos, "Optimised gettering and hydrogenation of multi-crystalline silicon wafers for use in solar cells," in *Proc. 22nd Eur. Photovoltaics Sol. Energy Conf.*, Milan, Italy, 2007, pp. 1309–1313.
- [9] M. D. Pickett and T. Buonassisi, "Iron point defect reduction in multicrystalline silicon solar cells," *Appl. Phys. Lett.*, vol. 92, pp. 122103-1–122103-3, 2008.
- [10] J. Hofstetter, J. F. Lelièvre, C. del Cañizo, and A. Luque, "Study of internal versus external gettering of iron during slow cooling processes for silicon solar cell fabrication," *Solid State Phenom.*, vol. 156–158, pp. 387–393, 2010.
- [11] M. Rinio, A. Yodyunyong, S. Keipert-Colberg, Y. P. B. Mouafi, D. Borchert, and A. Montesdeoca-Santana, "Improvement of multicrystalline silicon solar cells by a low temperature anneal after emitter diffusion," *Prog. Photovoltaics. Res. Appl.*, vol. 19, pp. 165–169, 2010.
- [12] D. Macdonald, A. Cuevas, A. Kinomura, Y. Nakano, and L. J. Geerligs, "Transition-metal profiles in a multicrystalline silicon ingot," *J. Appl. Phys.*, vol. 97, pp. 033523-1–033523-7, 2005.
- [13] T. Buonassisi, A. A. Istratov, M. Heuer, M. A. Marcus, R. Jonczyk, J. Isenberg, B. Lai, Z. Cai, S. Heald, W. Warta, R. Schindler, G. Willeke, and E. R. Weber, "Synchrotron-based investigations of the nature and impact of iron contamination in multicrystalline silicon solar cells," *J. Appl. Phys.*, vol. 97, pp. 074901-1–074901-11, 2005.
- [14] D. P. Fenning, J. Hofstetter, M. I. Bertoni, S. Hudelson, M. Rinio, J. F. Lelièvre, B. Lai, C. del Cañizo, and T. Buonassisi, "Iron distribution in silicon after solar cell processing: Synchrotron analysis and predictive modeling," *Appl. Phys. Lett.*, vol. 98, pp. 162103-1–162103-3, 2011.
- [15] D. Macdonald, S. Phang, F. Rougieux, S. Lim, D. Paterson, D. Howard, M. D. de Jonge, and C. Ryan, "Iron-rich particles in heavily contaminated multicrystalline silicon wafers and their response to phosphorus gettering," *Semicond. Sci. Technol.*, vol. 27, 125016-1–125016-5, 2012.
- [16] D. P. Fenning, J. Hofstetter, M. I. Bertoni, G. Coletti, B. Lai, C. del Cañizo, and T. Buonassisi, "Precipitated iron: A limit on gettering efficacy in multicrystalline silicon," *J. Appl. Phys.*, vol. 113, pp. 044521–044521, 2013.
- [17] R. Kvande, B. Geerligs, G. Coletti, L. Arnberg, M. D. Sabatino, E. J. Øvrelid, and C. C. Swanson, "Distribution of iron in multi-crystalline silicon ingots," *J. Appl. Phys.*, vol. 104, pp. 064905-1–064905-9, 2008.
- [18] G. Coletti, R. Kvande, V. D. Mihailitchi, L. J. Geerligs, L. Arnberg, and E. J. Øvrelid, "Effect of iron in silicon feedstock on p- and n-type multicrystalline silicon solar cells," *J. Appl. Phys.*, vol. 104, pp. 104913-1–104913-11, 2008.
- [19] J. Hofstetter, D. P. Fenning, M. I. Bertoni, J. F. Lelièvre, C. del Cañizo, and T. Buonassisi, "Impurity-to-efficiency simulator: Predictive simulation of silicon solar cell performance based on iron content and distribution," *Prog. Photovoltaics Res. Appl.*, vol. 19, pp. 487–497, 2010.
- [20] T. Trupke, J. Nyhus, and J. Haunschild, "Luminescence imaging for inline characterisation in silicon photovoltaics," *Physica Status Solidi (RRL)-Rapid Res. Lett.*, vol. 5, pp. 131–137, 2011.
- [21] J. Haunschild, M. Glatthaar, M. Demant, J. Nievendick, M. Motzko, S. Rein, and E. R. Weber, "Quality control of as-cut multicrystalline silicon wafers using photoluminescence imaging for solar cell production," *Sol. Energy Mater. Sol. Cells*, vol. 94, pp. 2007–2012, 2010.
- [22] B. Mitchell, H. Wagner, P. P. Altermatt, and T. Trupke, "Predicting solar cell efficiencies from bulk lifetime images of multicrystalline silicon bricks," *Energy Procedia*, vol. 38, pp. 147–152, 2013.
- [23] E. Scheil, "Bemerkungen zur Schichtkristallbildung," *Z. Metallkd.*, vol. 34, pp. 70–72, 1942.
- [24] G. Coletti, P. C. Bronsveld, G. Hahn, W. Warta, D. Macdonald, B. Ceccaroli, K. Wambach, N. Le Quang, and J. M. Fernandez, "Impact of metal contamination in silicon solar cells," *Adv. Funct. Mater.*, vol. 21, pp. 879–890, 2011.
- [25] J. Shur, B. Kang, S. Moon, W. So, and D. Yoon, "Growth of multicrystalline silicon ingot by improved directional solidification process based on numerical simulation," *Sol. Energy Mater. Sol. Cells*, vol. 95, pp. 3159–3164, 2011.
- [26] *Impurity-to-Efficiency (I2E) Simulator*, Mass. Inst. Technol., Cambridge, MA, USA, (2011). [Online]. Available: <http://pv-i2e.mit.edu/>
- [27] H. Wagner, T. Ohrdes, A. Dastgheib-Shirazi, B. Puthen-Vetttil, D. König, and P. P. Altermatt, "A numerical simulation study of gallium-phosphide/silicon heterojunction passivated emitter and rear solar cells," *J. Appl. Phys.*, vol. 115, pp. 044508-1–044508-6, 2014.
- [28] D. Macdonald, J. Tan, and T. Trupke, "Imaging interstitial iron concentrations in boron-doped crystalline silicon using photoluminescence," *J. Appl. Phys.*, vol. 103, pp. 073710-1–073710-10, 2008.
- [29] D. H. Macdonald, L. J. Geerligs, and A. Azzizi, "Iron detection in crystalline silicon by carrier lifetime measurements for arbitrary injection and doping," *J. Appl. Phys.*, vol. 95, pp. 1021–1028, 2004.
- [30] H. Wagner, M. Müller, G. Fischer, and P. Altermatt, "A simple criterion for predicting multicrystalline Si solar cell performance from lifetime images of wafers prior to cell production," *J. Appl. Phys.*, vol. 114, pp. 054501-1–054501-8, 2013.
- [31] A. Liu, Y.-C. Fan, and D. Macdonald, "Interstitial iron concentrations across multicrystalline silicon wafers via photoluminescence imaging," *Prog. Photovoltaics. Res. Appl.*, vol. 19, pp. 649–657, 2011.
- [32] A. Peral, J. Manuel Míguez, R. Ordás, and C. del Cañizo, "Lifetime improvement after phosphorous diffusion gettering on upgraded metallurgical grade silicon," *Sol. Energy Mater. Sol. Cells*, 2014. DOI: 10.1016/j.solmat.2014.02.026.
- [33] D. Macdonald, A. Cuevas, A. Kinomura, and Y. Nakano, "Phosphorus gettering in multicrystalline silicon studied by neutron activation analysis," in *Proc. IEEE 29th Photovoltaic Spec. Conf.*, New Orleans, LA, USA, 2002, pp. 285–288.
- [34] I. E. Reis, S. Riepe, W. Koch, J. Bauer, S. Beljakowa, O. Breitenstein, H. Habenicht, D. Krefner-Kiel, G. Pensl, J. Schön, and W. Seifert, "Effect of impurities on solar cell parameters in intentionally contaminated multicrystalline silicon," in *Proc. 24th Eur. Photovoltaic Solar. Energy Conf. Exhib.*, Hamburg, Germany, 2009, pp. 2144–2148.
- [35] T. U. Nærland, L. Arnberg, and A. Holt, "Origin of the low carrier lifetime edge zone in multicrystalline PV silicon," *Prog. Photovoltaics. Res. Appl.*, vol. 17, pp. 289–296, 2008.

- [36] A. A. Istratov, T. Buonassisi, R. J. McDonald, A. R. Smith, R. Schindler, J. A. Rand, J. P. Kalejs, and E. R. Weber, "Metal content of multicrystalline silicon for solar cells and its impact on minority carrier diffusion length," *J. Appl. Phys.*, vol. 94, pp. 6552–6559, 2003.
- [37] M. C. Schubert, J. Schön, F. Schindler, W. Kwapil, A. Abdollahinia, B. Michl, S. Riepe, C. Schmid, M. Schumann, S. Meyer, and W. Warta, "Impact of impurities from crucible and coating on MC-silicon quality—The example of iron and cobalt," *IEEE J. Photovoltaics.*, vol. 3, no. 4, pp. 1250–1258, Oct. 2013.
- [38] D. P. Fenning, A. S. Zuschlag, J. Hofstetter, A. Frey, M. I. Bertoni, G. Hahn, and T. Buonassisi, "Investigation of lifetime-limiting defects after high-temperature phosphorus diffusion in high-iron-content multicrystalline silicon," *IEEE J. Photovoltaics.*, vol. 4, no. 3, pp. 866–873, May 2014.
- [39] J. Chen, D. Yang, Z. Xi, and T. Sekiguchi, "Recombination activity of  $\sigma 3$  boundaries in boron-doped multicrystalline silicon: Influence of iron contamination," *J. Appl. Phys.*, vol. 97, pp. 033701–033701, 2005.
- [40] A. Liu and D. Macdonald, "Precipitation of iron in multicrystalline silicon during annealing," *J. Appl. Phys.*, vol. 115, pp. 114901–1–114901–10, 2014.
- [41] V. Kveder, M. Kittler, and W. Schröter, "Recombination activity of contaminated dislocations in silicon: A model describing electron-beam-induced current contrast behavior," *Phys. Rev. B*, vol. 63, pp. 115208–1–115208–11, 2001.
- [42] S. Castellanos, M. Kivambe, J. Hofstetter, M. Rinio, B. Lai, and T. Buonassisi, "Variation of dislocation etch-pit geometry: An indicator of bulk microstructure and recombination activity in multicrystalline silicon," *J. Appl. Phys.*, vol. 115, p. 183511–1–183511–7, 2014.
- [43] J.-F. Lelièvre, J. Hofstetter, A. Peral, I. Hocesc, F. Recart, and C. del Cañizo, "Dissolution and gettering of iron during contact co-firing," *Energy Procedia*, vol. 8, pp. 257–262, 2011.
- [44] D. P. Fenning, A. S. Zuschlag, M. I. Bertoni, B. Lai, G. Hahn, and T. Buonassisi, (2013). Improved iron gettering of contaminated multicrystalline silicon by high-temperature phosphorus diffusion. *J. Appl. Phys.*. [Online]. vol. 113, pp. 214504–1–214504–10. Available: <http://dx.doi.org/10.1063/1.4808310>
- [45] B. Michl, J. Schön, W. Warta, and M. C. Schubert, "The impact of different diffusion temperature profiles on iron concentrations and carrier lifetimes in multicrystalline silicon wafers," *IEEE J. Photovoltaics.*, vol. 3, no. 2, pp. 635–640, Apr. 2013.
- [46] J. Hofstetter, "Defect engineering strategies for solar grade silicon and their optimization by predictive simulation," Ph.D. dissertation, Dept. Phys. Electron., Univ. Politéc. Madrid, Spain, 2011.
- [47] J. Hofstetter, D. P. Fenning, J.-F. Lelièvre, C. del Cañizo, and T. Buonassisi, "Engineering metal precipitate size distributions to enhance gettering in multicrystalline silicon," *Phys. Status Solidi (a)*, vol. 209, pp. 1861–1865, 2012.
- [48] T. Buonassisi, A. Istratov, M. Marcus, B. Lai, Z. Cai, S. Heald, and E. Weber, "Engineering metal-impurity nanodefects for low-cost solar cells," *Nature Mater.*, vol. 4, pp. 676–679, 2005.

Authors' photographs and biographies not available at the time of publication.